An investigation of mechanical and electrical properties of friction stir welded Al and Cu busbar for battery pack applications

Omkar Mypati, Suryakanta Sahu, Surjya Kanta Pal*, Prakash Srirangam

Department of Mechanical Engineering, Indian Institute of Technology Kharagpur, 721302, India

Omkar Mypati, Surjya Kanta Pal

Advanced Technology Development Centre, Indian Institute of Technology Kharagpur, 721302, India.
Suryakanta Sahu

Warwick Manufacturing Group, University of Warwick, CV4 7AL, UK
Prakash Srirangam

**Corresponding author: skpal@mech.iitkgp.ac.in*

Abstract:

The aluminum and copper (Al-Cu) busbar is widely used as a core component in Lithium-Ion (Li-ion) batteries. The Al-Cu busbar is challenging to fabricate with the traditional welding processes because of its high thermal conductivity. The Al-Cu busbar is fabricated using the friction stir welding method in the present study. The effect of temperature and vibration generated during the welding process on intermetallic compounds (IMCs) is studied using the effective formation model and found that Al_2Cu is the first to form at the interface. The IMC formation at the joint interface had detrimental (Al-rich IMC) and beneficial (Cu-rich IMC) effects. The presence of detrimental IMCs affects the joint strength of about 36 % as compared to the sample with the highest tensile load. The surface electrical conductivity is measured by using a Gaussian profile method and found in the range of 0.94 – 5.37 μ Ω·mm. The welded samples with the presence of Al_2Cu_3 and Al_4Cu_9 IMC at the interface are found to have higher electrical conductivity. Interestingly, the sample with a higher tensile load had observed higher electrical conductivity due to the formation of Cu-rich IMC, i.e., Al_4Cu_9.

Keywords: Al-Cu joints, busbar, li-ion batteries, intermetallic compounds, electrical resistivity

1 Introduction

Nowadays, the usage of electric vehicles (EVs) rather than internal combustion (IC) engine vehicles is scaled up due to their high efficiency, no emission of CO_2 gas, reduction of engine noise, and low maintenance cost [1]. Considering those many advantages, customers are inclining towards the EVs. In earlier days, batteries are used to provide power for all electrical components in automobiles [2–4]. But nowadays, research on batteries has been increased to a great extent to increase efficiency and specific energy. These days, various types of batteries have been used in EVs, such as lead-acid, nickel-metal hybrid, and lithium-ion battery [5, 6]. The physical quantities of the batteries, as stated in Table 1, are capable enough to generate power for running an automobile. Lead-acid batteries have a disadvantage of a maximum temperature limit of about 25^0C. Due to this constraint, these batteries are exhausted for EVs. The specific energy for NiMH battery is comparatively less than Li-ion battery due to less voltage [7]. The energy generated by the battery depends on the capacity and the voltage, as shown in Equation 1 [7].

$$E_b = c_{\,b} \times v_b, \tag{1}$$

where, E_b= Energy, $c_{\,b}$= Capacity, and v_b= Voltage of the battery

The Specific energy of the battery can be calculated by using Equation 2 [7].

$$S_e = \frac{E_b}{u_c}, \tag{2}$$

where, S_e= Specific energy, u_c = Volume (cylindrical or rectangular shape) of the battery

Most of the EVs are equipped with cylindrical cells combined with series and parallel, schematically shown in Fig 1 [4]. The S_e is directly proportional to the voltage of the battery where volume and capacity of the battery is kept constant. Higher the v_b, EVs can go faster and they can achieve the speed of IC engine vehicles. Among them, lithium-ion batteries are being extensively used [8, 9] because of their high specific energy, i.e., nearly 0.36 to 0.875 MJ/kg compared to other batteries [4, 8, 10].

Table 1: Types of batteries used in EVs, with their physical quantities [4, 8, 10]

Battery Type	Specific energy (Wh/Kg)	Specific density (Wh/L)	Efficiency (%)
Nickel–metal hydride battery (NiMH)	60- 120	140-300	66-92
Lead acid	33-42	60-110	50-95
Li-ion battery	100-265	250-693	80-90

These battery cells are combined either in series or parallel to form a battery pack. A bunch of one terminal battery cell is connected with another terminal using a busbar to continuously transmit current to the electric motor in EVs [4]. The electrical busbar is available in rectangular, round, and cross-sectional shapes. The busbar is used to achieve the desired voltage and responsible for power transmission. Generally, electronic materials like copper and aluminium have been used to manufacture busbar [11], as shown in Fig. 2.

Moreover, the high-efficiency battery pack causes problems like short circuits. Many of such failures are observed in the busbar. The failures are mainly due to Kirkendall voids formed during improper joining or diffusion of aluminium and copper [12]. Another reason is while running the EVs, and vibrations are generated during the up and downs, which causes fatigue failures in the busbar [13]. The fabrication of a busbar has become a challenge for the automobile industry.

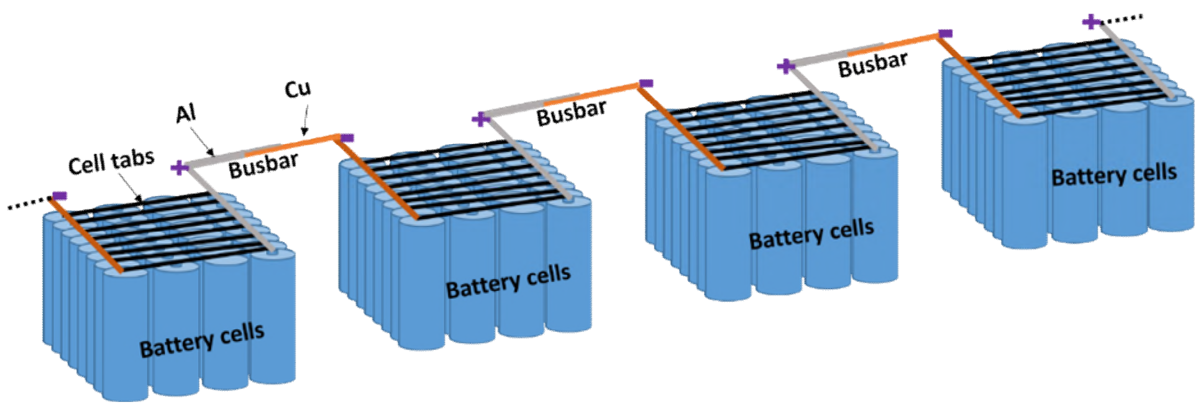

Fig 1. Schematic of a battery pack

However, the busbar can be fabricated using mechanical fasteners (riveting) and different welding methods [14, 15]. Riveting methods are prominently used in battery packs due to the easy joining of dissimilar materials [4]. But the fastening has limitations, such as the exposure of the joint interface to air, leading to moisture accumulation, which may lead to failure due to thermal defect and corrosion persistence for an extended period. The busbar materials need to be welded to reduce thermal failures and increase electrical conductivity. Al and Cu, being dissimilar materials have different physical properties such as density, melting point, thermal conductivity etc, it is challenging to welded these metals to welded these metals using traditional fusion welding methods. High amount of heat is required to weld Al to Cu due to presence of oxides over the Al base metal. Fusion welding of Al and Cu result in various problems such as high-stress concentration, formation of brittle IMCs due to the high heat input. Such IMCs in the weld zone affect mechanical and electrical properties, like decreased tensile strength, an increase in microhardness, and a reduction of electrical conductivity, respectively [16, 17]. Moreover, the welded busbar essentially needs to be defect-free. It must have desirable mechanical, metallurgical, and electrical properties to sustain high voltage, temperature, and vibrations during the running of the EVs [12].

Concerning this problem, various advanced joining and welding processes for dissimilar materials, i.e., brazing, laser welding, and friction stir welding (FSW), have been used. The direct heat exposure in brazing of Al and Cu joints leads to the thinning of the weld interface and formation of brittle IMC like the Al_2Cu phase. There is always weld thinning at the joints in conventional FSW or its derivations. The thinned area is caused by shoulder plunges into the workpiece to a specific thickness, where frictional heat is generated and the plasticized materials overflow. The thinning of the weld interface causes flash defects, reducing the effective load-bearing area and decreasing mechanical properties [18]. As stated earlier, brittle IMCs in the welding zone lead to crack initiation at lower tensile or fatigue load. To minimize the brittle IMCs, an external filler needs to be added. Filler metal Zn-15Al observed the highest shear load [19]. However, extra filler materials in the brazing process increase the heat affected zone (HAZ), which will degrade the electric properties. To minimize the HAZ of the welded sample, an advance solid-state welding process has emerged. In this regard, laser welding has significant importance in the joining of dissimilar combinations. However, laser welding has some limitations, i.e., high reflectivity materials like Al are hard to weld. Higher heat input is needed for the joining of highly reflective materials. The higher heat input also leads to the formation of harder IMCs, i.e., Al_2Cu and CuAl, resulting from decreasing in the ultimate tensile strength (UTS) [20]. Researchers have adopted filler materials to enhance the tensile load, i.e., $AlSi_{12}$ and $CuSi_{3,}$ during the welding process [21]. The filler materials decrease the formation of harder IMCs by maintaining a uniform distribution of Cu concentration, which leads to the formation of Cu-rich IMCs. The laser welds performed with $AlSi_{12}$ exhibit the highest tensile strength compared to $CuSi_3$, where the welded samples without filler material observed the lowest tensile strength [21].

In the current study, the aluminium-copper busbar has been fabricated by using FSW [22, 23]. The FSW samples have also been reported to have excellent mechanical properties, i.e., tensile strength, fatigue, microhardness, etc., and metallurgical properties, i.e., grain size, corrosion, etc., as compared to other solid-state welding processes. This FSW process is done by using friction as a heat source created by employing a tool. FSW tool consists of two main parts, i.e., shoulder and pin, as shown in Fig 2. The shoulder part creates frictional heat, which causes plastic deformation of material [24]. The pin portion stirs the plastically deformed material and leads to material mixing between two dissimilar materials and makes joint, as shown in Fig. 3. With the joining of Al-Cu, researchers suggested placing Cu below the Al sheets to reduce the tool wear and generate more heat at the weld interface [25]. Besides, the diffusion of Cu in Al is more than the Al in Cu [26].

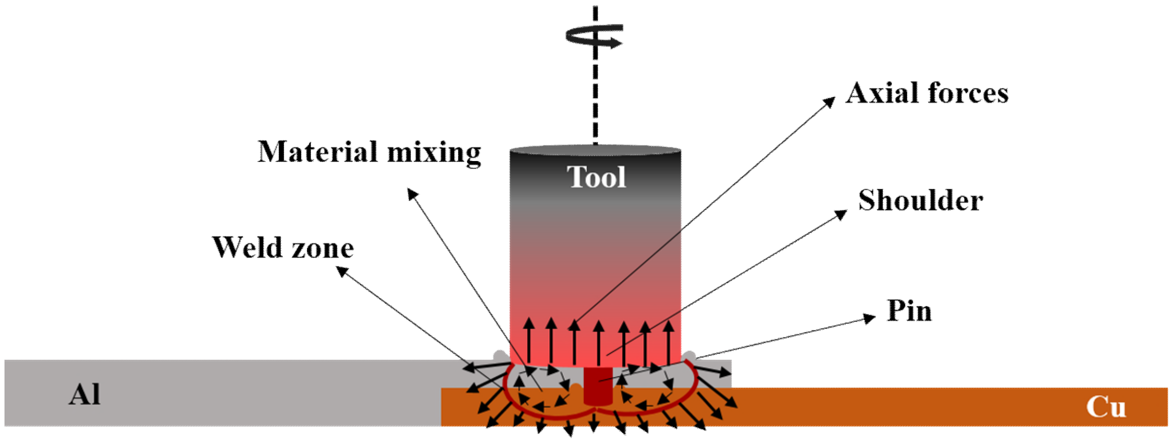

Fig 2. Schematic of FSW of Al-Cu busbar

The process parameters of FSW are rotational speed (ω), weld speed (*v*), plunge depth (PD), and tilt angle (α). The ω, and *v* involved in generating heat input and change in α enhance the material mixing, which leads to high joint strength. The optimization of process parameters produces a sound weld in both similar and dissimilar combinations of joining [23, 27]. Based on heat generation IMCs are formed accordingly to the diffusion of aluminium and copper. As temperature increases, the reaction between Cu and Al increases, resulting in a higher diffusion rate, leading to more IMCs. Generally, IMCs like Al_4Cu_9, AlCu, and $AlCu_4$ are formed at the weld interface. The Al-rich IMCs are harder and brittle leading to lower UTS of welded samples, as mentioned earlier. The material mixing plays an important role in reducing the voids in the weld interface [8]. The presence of voids at the interface decreases the mechanical strength and leads to thermal failures in the busbar application. However, copper-rich IMCs at the weld interface is highly conductive for heat and electricity [8, 12]. During welding of Al and Cu, the weldments exhibit highly reactive and fast oxides formation, increasing resistivity.

In addition to the study of mechanical and metallurgical properties of the weldments, the current study also focused on the electrical properties, which are essential for battery applications. Electrical resistivity is influenced by the presence of IMC in the welded joints. Hence, the study focuses on the effect of IMC on mechanical properties and electrical resistivity. The electrical resistivity is measured at different temperatures from 300 K to 345 K.

2 Materials and methodology

The busbar is fabricated by joining base materials of pure Al and Cu with the dimensions of 100 mm x 80 mm. A 3 mm thick Al is milled up to 1 mm at the weld zone and placed over a Cu sheet of 2 mm thick in an overlapping configuration, with an overlap distance of 30 mm, as shown schematically in Fig. 3. The FSW has been carried out using a tool made of H13 tool steel with a shoulder diameter of 16 mm, pin diameter of 5 mm, and a pin height of 1 mm. The process parameters used in the welding process are listed in Table 2. The welding experiments were carried out using an FSW machine (WS004, ETA Bangalore). The thermocouples were connected to a data acquisition card (NI 9211) to acquire the temperature signals. In the advancing and retreating sides of the weld samples, two K-type thermocouples were placed 1 mm away from the shoulder's periphery, as shown in Fig.3 (a). A 3-axis accelerometer (ADXL335) module is placed near the welded sample, and the vibration signals are acquired from the sensor by using a microcontroller, as shown in Fig. 3 (a).

Table 2. Process parameters with sample nomenclature

Sample nomenclature	**S_1**	**S_2**	**S_3**	**S_4**	**S_5**	**S_6**	**S_7**	**S_8**	**S_9**	**S_{10}**	**S_{11}**	**S_{12}**
***ω* (rpm)**	1600						2400					
***v* (mm/min)**	60		120		200		60		120		200	
***PD* (mm)**	0.1	0.2	0.1	0.2	0.1	0.2	0.1	0.2	0.1	0.2	0.1	0.2

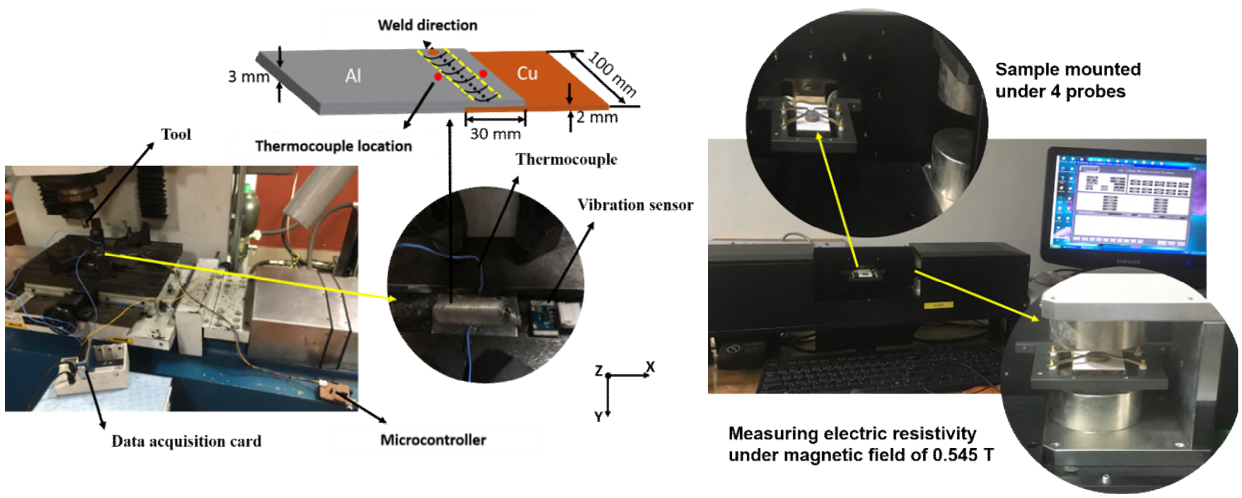

(a) **(b)**

Fig 3. Experimental setup (a) weld schematic, and (b) electrical conductivity

The UTS of the welded samples is evaluated using a universal tensile machine (Instron, 8862), where the base materials Al and Cu have UTS values of 82.01 MPa and 219.9 MPa, respectively. The metallurgical characterization of the welded samples was performed by cutting the samples in the dimension of 25 mm × 8 mm. The samples were then mounted using a hot mounting press (Struers, Citopress). The mounted specimens were polished by using a sample grinding and polishing machine (Struers, Labopol 30). The microstructure was found using Leica Microsystems, DMi8A) and microhardness using UHL, VMHT 001). The microhardness of the base Al and Cu is found to be 68 HV and 95 HV, respectively. The IMCs at the weld interface have been identified using an X-Ray diffraction machine (PANalytical B.V, 7602 EA) with Cu anode and maintaining a voltage of 40 kV a current of 40 mA within a range from 20° to 120°. The hardness of IMC is measured by using a nanoindentation instrument (Anton Paar, NHT). The electrical resistivity of the welded samples is measured by using a 4-probe electrical conductivity setup (Ecopia, 0.545T), as shown in Fig. 3 (b). The electrical resistivity was measured with varying temperatures from 300 K to 345 K.

3 Results and discussion

3.1 Temperature signals

The temperature generated during the welding process significantly affects the plastic deformation and the formation of IMCs at the weld interface. Generally, the plasticity changes rapidly once the temperature goes above the critical temperature [28], which concludes an increase in peak temperature increases metal plasticity. Due to very high plasticity in the welded sample leads to poor material mixing, leading to a decrease in weld quality. Similarly, in FSW lap joints of AA5083 and SS400, the increase in the diameter of tool pins and tool tilt angle results in larger voids along with the weld interface [29]. A reduction in peak temperature generation tends to void formation due to a lack of plasticization of materials. Therefore, optimisation of process parameters is essential for good quality welds. Fig 4 (a) depicts, at constant ω of 2400 rpm with the increase in v from 60 mm/min to 120 mm/min, there is a decrease in temperature, which is due to the reduction in the contact time of the tool with a workpiece. A similar result was observed from 120 mm/min to 200 mm/min. Fig 4 (a) shows the maximum peak temperature attained in sample S_{11} is faster than samples S_9 and S_7 due to the quick movement of the tool along the welding zone. Fig 4 (b) depicts at a constant v of 60 mm/min and the increase in ω from 1600 rpm to 2400 rpm there is nearly 36.5 % increase in temperature due to more frictional heat generation. However, Fig 4 (c) shows with the increase in *PD*, the contact surface area of the tool with the workpiece increases, leading to more heat generation. It is also observed that the rise in temperature for sample S_2 is about 16.9 % as compared to sample S_1.

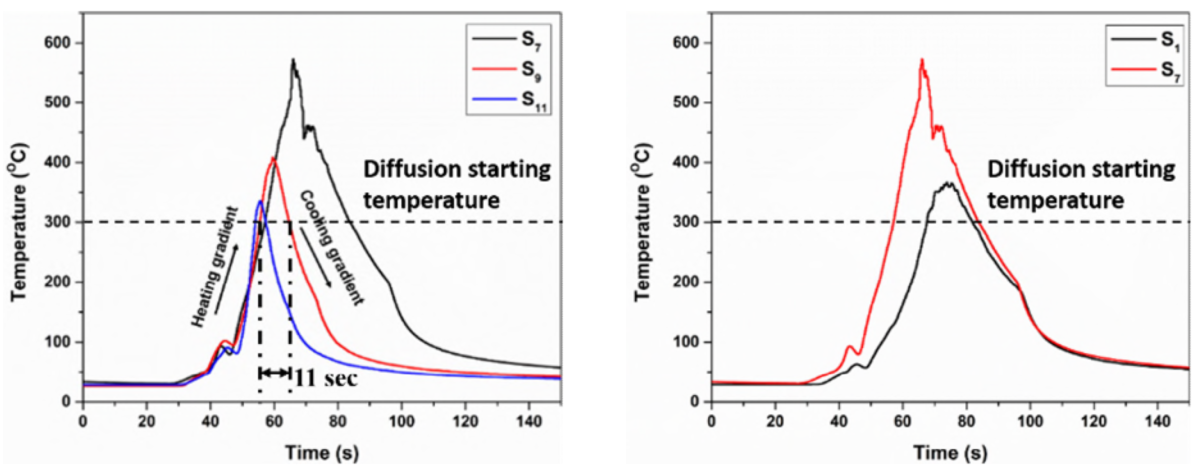

(a) (b)

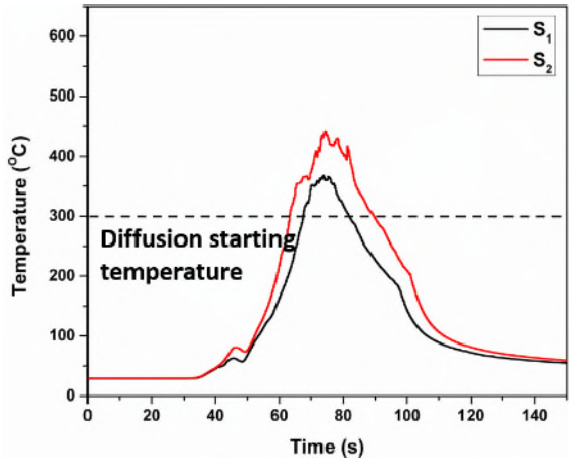

(c)

Fig 4. Variation of temperature with respect to (a) *v* at constant *ω* of 2400 rpm, (b) *ω* at constant *v* of 60 mm/min, and (c) *PD* at constant *ω* of 1600 rpm

The generation of peak temperature has a significant effect on the diffusion of Al and Cu at the weld interface. Fig 5 depicts the phase diagram generated by using a Thermocalc software for Al-Cu, which determines the solubility of Cu in Al. The diffusion of Al-Cu is starting nearly about the temperature at 300 ^{o}C to from the IMC. The details about the formation of various IMCs and corresponding diffusion coefficients are explained in the below sections.

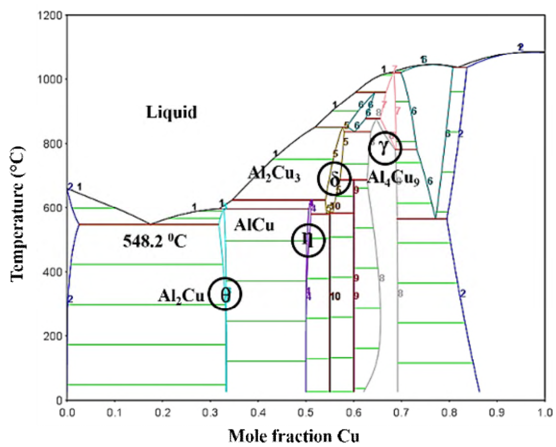

Fig 5. Binary equilibrium phase diagram of Al-Cu determining IMC phases

3.2 Vibration signals

Fig. 6 shows the vibration signal of the FSW process, which has refraction and compression. The variation in the vibration signal along the 3 axes has been measured for sample S_1. Fig 6 (a) depicts vibration along the X-axis, which has more amplitude of vibration than the Y-axis and Z-axis, but there is no significant relation with the process. The signal along the Y-axis is represented in Fig 6 (b), which can only be correlated with the FSW process. Fig 6 (b) is divided into five regions. In region 1, the vibration is very low, owing to the machine being in an idle state. Region 2 has higher vibration levels due to the plunging of the tool, whereas in region 3, it decreases due to dwelling. The vibrations level further increases during the welding operation, which can be observed in region 4, and after completion of welding, region 5 depicts the idle condition of the machine. The vibration along the Z-axis has no significant correlation with the welding process, and the same is illustrated in Fig 6 (c).

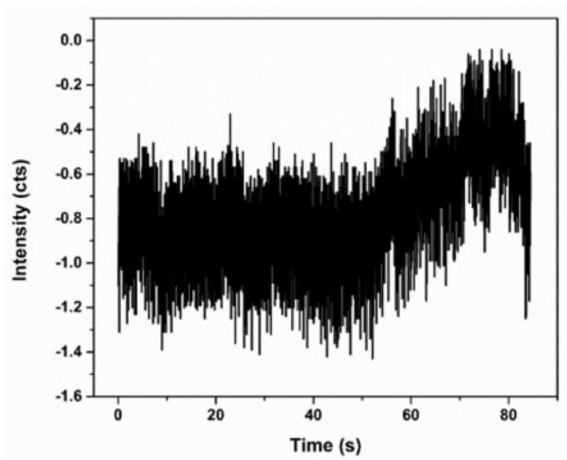

(a)

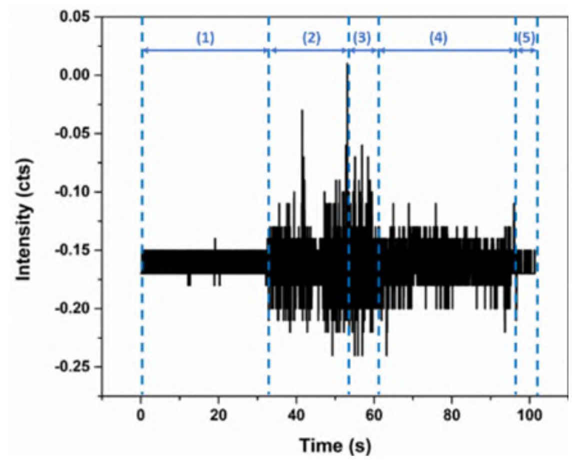

(b)

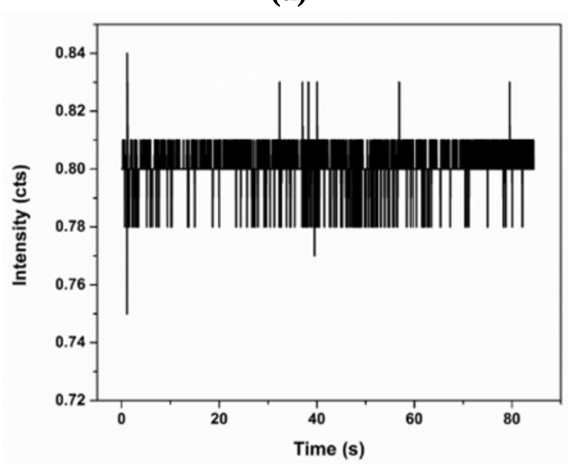

(c)

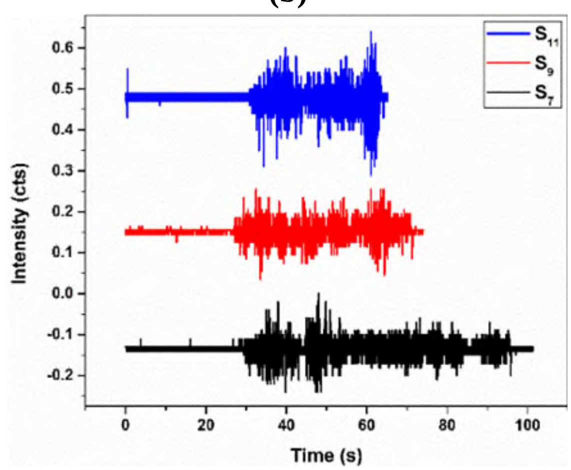

(d)

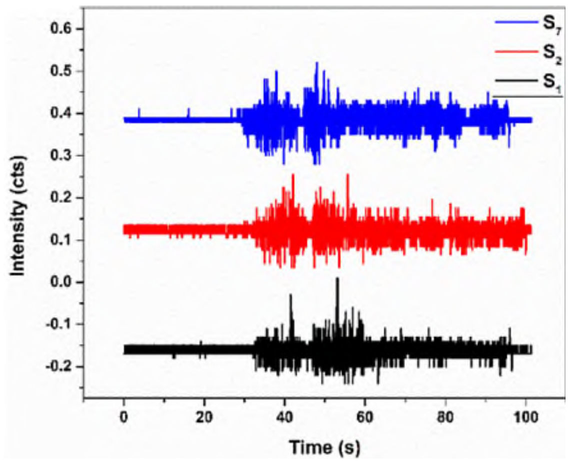

(e)

Fig 6. The vibration of signals of sample S_1 along the 3-axis; (a) X-axis, (b) Y-axis, (c) Z-axis, vibration signals varying with (d) *v*, and (e) ω and *PD*

The variation of vibration intensity with respect to *v* is shown in Fig 6 (d). The vibration intensity of the welding at 50 mm/min is less than 150 mm/min, similarly at 200 mm/min. As mentioned earlier, at lower welding speed, the temperature generation is high and leads to softening of the material, which reduces the interaction force between tool and workpiece. The decrease in the interaction force reduces the vibration intensity. It can be concluded that with the increase in *v*, the intensity of vibration in the welding increases.

Similarly, with higher ω, and *PD*, larger is the heat generation, leading to less vibration, as depicted in Fig 6 (e). The change in process parameters influences the intensity of vibration during the welding operation. However, higher internal vibrations enhance the Cu to rupture into fragments from the interface and mix with the Al matrix at the weld zone. Hence, the vibration generated during the welding process also significantly affects the formation of Cu-rich IMCs at the weld interface.

3.3 Weld interface analysis: quantification of elemental composition at the weld zone

Fig 7 depicts the macro images of all the samples at the weld zone along with an elemental mapping analysis and microstructure of Cu at the weld nugget zone. The study results about the weld morphology at the welding interface. The formation of hook in the FSW samples is patchy, and greater hook size is observed at the AS [30, 31]. The plasticized material of Al flows from AS to RS, where more plastic deformation occurs at the AS. Hence, the greater hook size has been observed at the AS. A study on hook formation and its height is needed for a good quality weld. The hook height increases with an increase in *PD*. Fig 7 (a) and (b) show the hook height is double i.e., sample S_1 (252.6 μm) to sample S_2 (518.6 μm). The hook height variation in the samples S_1 and S_2 is mainly due to the excess Cu material penetrating the Al matrix because of the forging action on Cu by the FSW tool. The hook height increases with the increase in ω at constant *PD* and *v*, as shown in Fig 7 (a) and (c). With an increase in ω, the tendency of Cu penetration into the

Al matrix is higher due to severe plastic deformation at higher temperatures. Hence, the hook height is greater for sample S_7 (282.2 μm) than sample S_1 (252.6 μm).

Similarly, with an increase in *v*, the heat generation decreases, and the penetration of Cu is rigid into the Al matrix. Hence the hook height is reduced from sample S_7 (282.2 μm) to S_9 (247.4 μm) and S_{11} (218.4 μm). Besides, the Cu fragments are detached at the weld interface with an increase in *v* due to insufficient heat generation and improper material mixing. The quantitative study of the weld interface is essential for electrical applications, mainly at power transmission. In this regard, the weld interface is scanned to get the element composition. Since the diffusion of Al-Cu has occurred mainly in the nugget zone hence, the weld nugget zone is considered for the analysis by considering a constant 5 mm x 3 mm area for all the samples. The percentage of Al and Cu composition is shown in Fig 7 (f), and it is obtained from the elemental mappings as represented in Fig 7. At lower *ω*, the composition of Cu is found to be low due to effective material mixing and insufficient heat generation for severe plastic deformation. The presence of more Cu at the weld interface determines the good electrical properties for the given weld parameters. The samples $S_{8,}$ S_7, and S_9 have the equivalent Al and Cu percentage in the decreasing order at the weld nugget zone. The process parameters of the three welded samples mentioned above are suitable for producing a good amount of Cu composition at the interface, which is essential for the busbar application.

The grain structure effect is mainly due to the cooling gradients obtained during the welding process and shown in Fig 4 (a). It also depicts the grain size for the Cu at the welded nugget zone, and it is observed that the grain size decreases with an increase in v. The steeper the cooling gradient, the faster is the cooling rate. For Sample S_{11}, the gradient is steeper than Samples S_7 and S_9, as shown in Fig 4 (a). Besides, microstructure images in Fig 7 depict the fragmentation of Cu increases with an increase in *v*, which may enhance the tendency to form the Cu-rich IMC. The sample S_7 shows a larger grain size due to a slower cooling rate than the sample $S_{1,}$ as shown in Fig 4 (b).

Similarly, with the increase in *PD*, the heat generation increases and observes a slower cooling rate, increasing the grain size. The microstructure study of the Cu at the weld interface is necessary, where the effect of grain boundary directly impacts the electronic property of the welded joint. The grain boundary acts as a potential barrier with a low ionic density, leading to restriction in electron flow [32]. Hence, the potential barrier scatters the electrons during the conduction, which led to an increase in the electrical resistivity

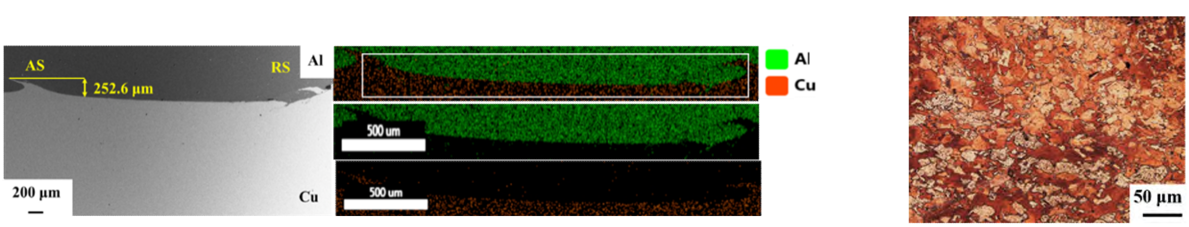

(a)

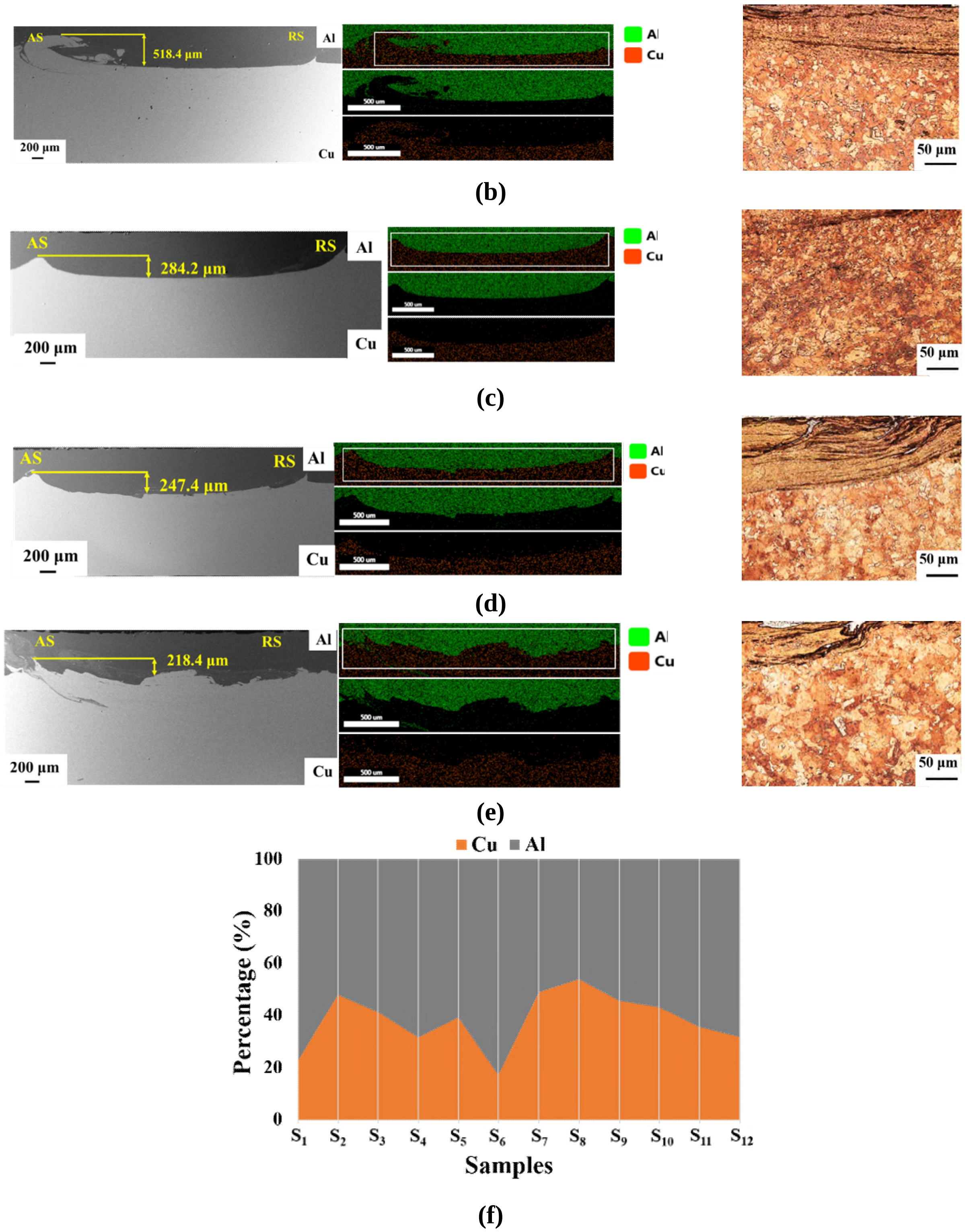

Fig 7. Weld interface study indicating the nugget zone microstructure for the samples (a) S_1, (b) S_2, (c) S_7, (d) S_9, (e) S_{11}, and (f) elemental quantification for all the welded samples

The microstructure of the welded samples has a significant effect on microhardness. Thus, the average microhardness has been correlated with the average grain size, as depicted in Fig 8 (a). the results has been reported [33], the samples with lesser grain size have higher microhardness. Fig 8 (b) shows the microhardness for the welded samples measured along the thickness direction with varying ω. Fig 8 (b) is divided into 3 zones; zone 1 depicts the hardness of Al in the weld nugget, zone 2 refers to the diffusion of the Al-Cu interface, and IMC zone at this weld interface. Zone 3 depicts the hardness of Cu. The microhardness of sample S_1 is greater than sample S_7 due to a faster cooling rate at lower ω, leading to higher microhardness.

Fig 8 (c) and (d) depict the microhardness for the welded samples with varying *PD* and *v*, respectively. S_1 has higher microhardness as compared to S_2 due to higher *PD.* With the increase in ω and *PD,* the heat generation increases, leading to coarsening of grains and a decrease in the microhardness. Fig 8 (d) depicts that microhardness increases with an increase in *v*, which is due to the formation of fine grains at the weld interface owing to a faster cooling rate.

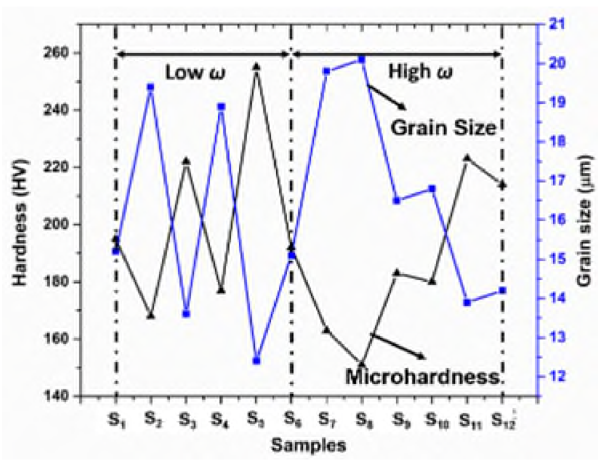

(a)

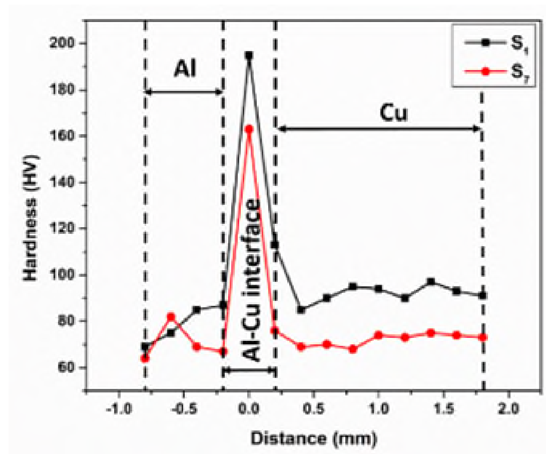

(b)

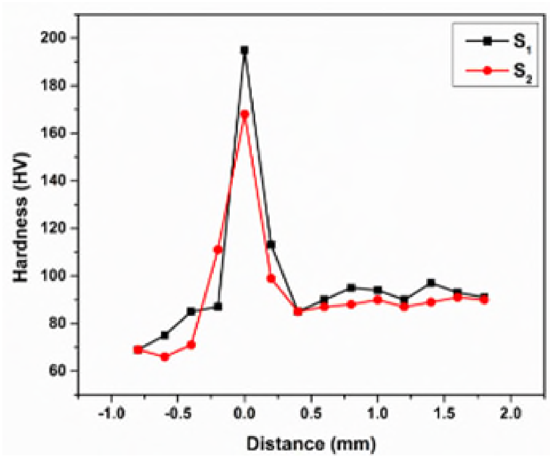

(c)

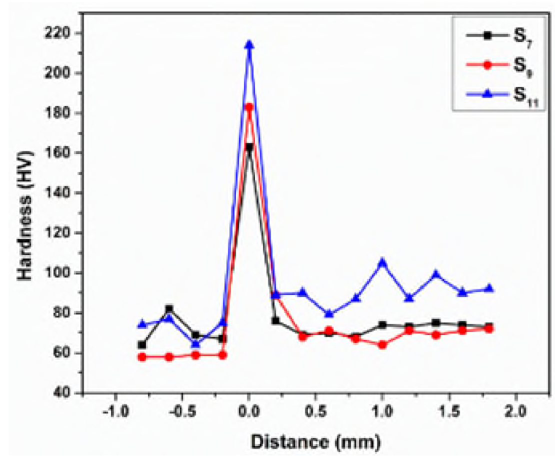

(d)

Fig 8. (a) Variation of average hardness and grain size, and microhardness variation with; (b) *ω*, (c) *PD*, and (d) *v*

3.4 Tensile strength

The mechanical properties such as UTS depend on hook height and the IMCs phase and composition. As mentioned earlier, the formation of IMC is related to the temperature generated during the welding processes. In this context, ω and v have a vital role in the formation of IMCs. Fig 9 (a) depicts UTS variation for different process parameters, where it is observed that S_9 has the highest UTS. The variation in the UTS is studied based on the IMC formed at the weld interface of Al-Cu. However, both Al and Cu materials have different intermixing rates [34, 35]. The major IMCs formed at the interface are AlCu, Al_2Cu, Al_2Cu_3, and Al_4Cu_9. Among them, Cu-rich IMC is favourable for the improvement in joint strength which forms due to a short supply of Al during solidification [36, 37]. The ω/v ratio has considerable control over the heat generation. As a result, an increase in ω increases frictional heat and initiates effective plastic deformation. Higher v generates less heat input, which decreases the diffusion of Al and Cu, leading to the formation of Al-rich IMC, where these IMC deteriorates the joint strength. Figs 9 (b), (c), and (d) depict various IMC formation by varying v, and it was observed that at lower v, the intensity of IMC peaks was higher. The phase formed in S_1 at a lower angle was Al_2Cu_3, as shown in Fig 9 (b), where sufficient heat was generated and caused higher diffusion. Still, for samples S_3 and S_5, the IMC Al_2Cu was found due to diffusion owing to insufficient heat generation, as represented in Fig 9 (c) and (d). Thus, there is a direct relation between the heat input and formation of IMCs, i.e., with an increase in ω, there is an increase in IMC formation with higher intensity. A higher UTS of 54 MPa was found in the sample S_9 due to the formation of Cu-rich IMCs, i.e., Al_2Cu_3 and Al_4Cu_9. As mentioned earlier, the optimum internal vibrations in the welded samples is generated during higher v, assisted to the formation Cu-rich IMC i.e., Al_4Cu_9 is formed, and the same can be observed from Fig 9 (b), (c), and (d). The Al_4Cu_9 IMC enhances not only the tensile strength but also electrical properties, which is discussed in later sections.

Moreover, the sample with high microhardness at the Al-Cu interface zone exhibits a brittle nature and observed lesser UTS. The sample S_8 generates a maximum temperature of 579 ^{o}C during the welding process causes a higher microhardness of 258 HV, which has been observed to have a lower UTS of 21.27 MPa. The samples with higher ω have more plastic deformation leading to an increase in 4.78% of UTS for the sample S_7 as compared to S_1. *S*imilarly, the UTS of sample S_9 was 26% more than sample S_3. As mentioned earlier, more Cu fragments in the Al matrix resulted in a decrease in the UTS, where sample S2 observed a reduction in UTS of 39.54% compared to S_1. Figs 9 (e) and (f) depict the fracture surface of sample S_1 and S_2, respectively, where Fig 9 (f) has more Cu fragments embedded in the matrix, which result in a decreasing tensile strength.

The fracture morphology of all the welded samples is depicted in Figures 9 (e) to (p). The facture joints exhibit tearing ridges, river patterns, ductile cracks, and various dimples like shear and equal-axis. In the samples at *v* of 60 mm/min and 120 mm/min, the quasi-cleavage fractures are observed, and the same has been shown in Fig 9 (e), (f), (g), (h), (k), (l), (m) and (n), respectively. However, in the FSWed samples with higher *v*, i.e., at 200 mm/min, the brittle fracture surface morphology has been observed and mentioned in Fig 9 (i), (j), and (p), respectively. The sample S_{11} exhibits ductile cracks, which is contradicting the above statement. The heat generated is not sufficient for proper plastic deformation of Al and Cu; hence the ductile cracks are initiated, which led to intergranular fracture. Fig 9 illustrates the fracture of the Al and Cu welded joints caused by stress; accordingly, the formation of dimples varied in the fracture morphology. The sample with normal tensile stress observed equal-axis dimples, where the samples undergo shear stress, which leads to the formation of shear dimples.

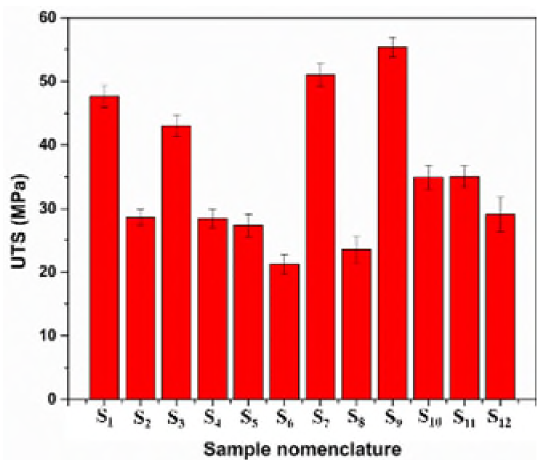

(a)

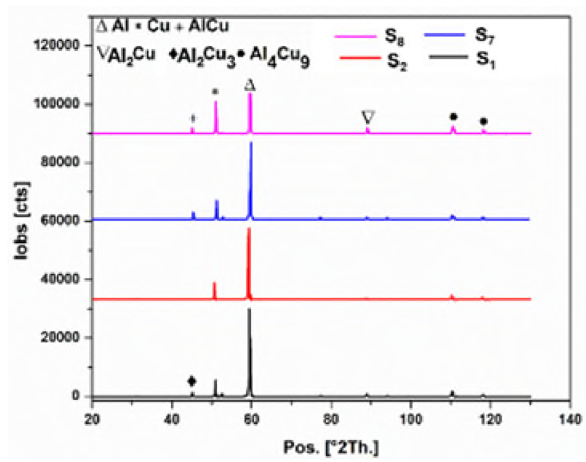

(b)

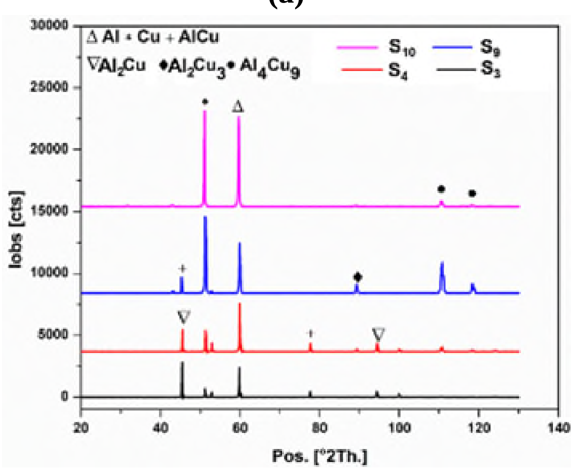

(c)

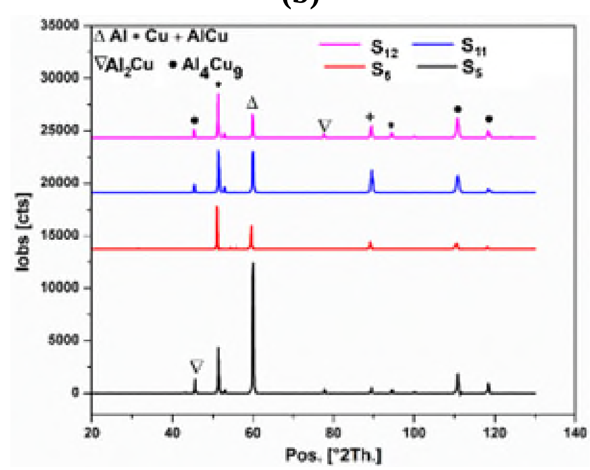

(d)

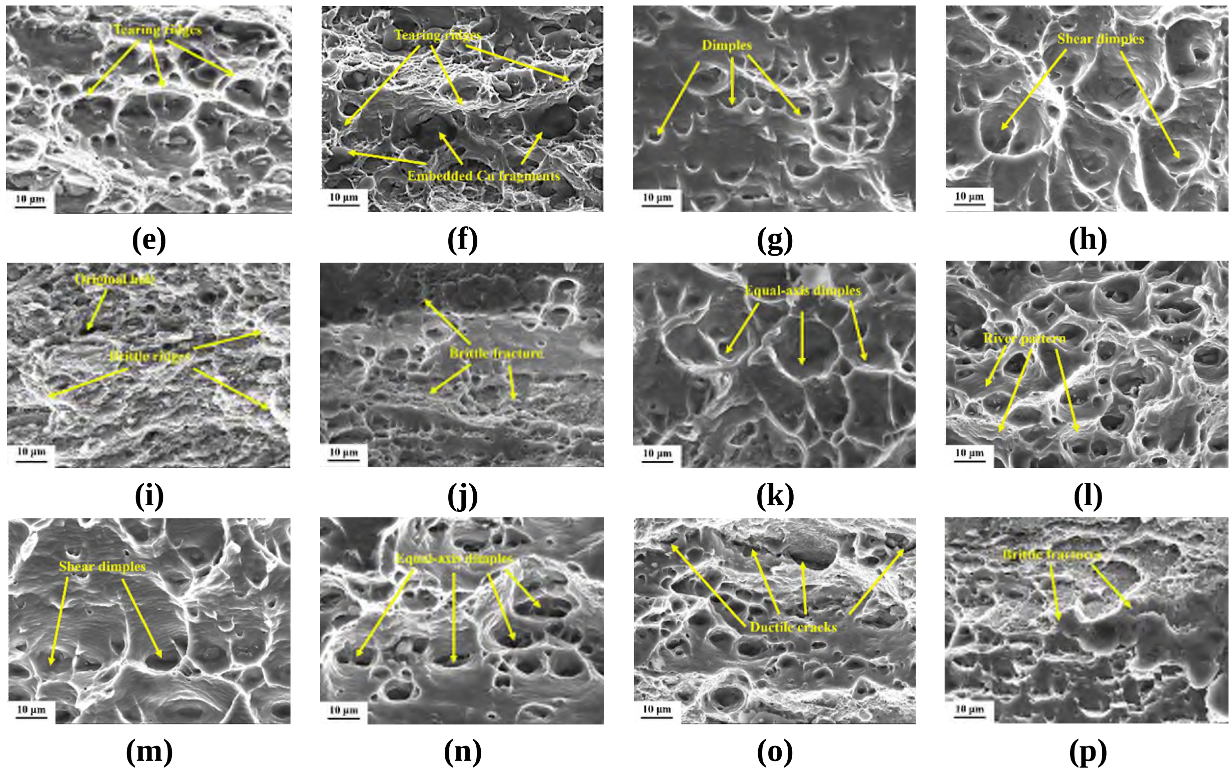

Fig 9. (a) variation of UTS and variation of XRD with respect to *v*; (b) 60 mm/min, (c) 120 mm/min, and (d) 200 mm/min, fratograpy for the samples (e) S_1, (f) S_2, (g) S_3, (h) S_4, (i) S_5, (j) S_6, (k) S_7, (l) S_8, (m) S_9, (n) S_{10}, (o) S_{11}, and (p) S_{12},

3.5 IMC formation and thickness:

The formation and growth of Al-Cu IMC are mainly due to chemical reaction (thermodynamical model) and diffusion (kinetic model) via thermal and mechanical cycles during the welding process.

The sequence of IMC formation has been studied using the thermodynamic model, i.e., effective heat of formation (E_{HF}). Additionally, the change in Gibbs energy (ΔG) represents the driving force for the chemical reaction [38].

$$\Delta G = \Delta H - T \times \Delta S \tag{3}$$

where, ΔG is the Gibbs free energy, ΔH is the enthalpy change, ΔS is entropy change, and T is the temperature.

[38] mentioned in the FSW process, as a result of the severe plastic deformation, dynamic recrystallization grains form near the interface between the tool and the workpiece, resulting in adiabatic heating. Hence, the change in heat transfer is considered as approximately zero. Finally, the change in entropy is nearly zero. So, the product of temperature and change in entropy is approximately zero. The change in Gibbs energy can be written as a change in enthalpy:

$$\Delta G \approx \Delta H \tag{4}$$

[38] explained E_{HF} model assumes the chemical reaction at an effective concentration of elements at the weld interface, where IMC growth occurs. Hence, the effective heat for the formation of E_F as $\Delta H'(T)$ has been considered for every IMC formed at the interface.

$$\Delta H'(T) = \Delta H^0(T) \times \frac{C_e}{C_l} \tag{5}$$

where, $\Delta H^0(T)$ is the change in enthalpy or the heat of formation at a given temperature, C_e is the effective concentration of limiting element, and C_l is the compound concentration of the limiting element.

The $\Delta H^0(T)$ for different IMCs are calculated, as shown in Equations 6, 7, 8, and 9 using the Gibbs free energy curves generated with Themocalc software. The curves are drawn from the software by varying temperature from 450 °C to 600 °C. The specified range is considered because for better accuracy of the Gibbs free energy, the peak temperature of all the weld samples is lying in the temperature mentioned above.

$$\Delta H^0(T)(Al_2Cu) = -14396 + 1.55T \tag{6}$$
$$\Delta H^0(T)(AlCu) = -21239 + 3.68T \tag{7}$$
$$\Delta H^0(T)(Al_2Cu_3) = -17354 - 2.84T \tag{8}$$
$$\Delta H^0(T)(Al_4Cu_9) = -16957 - 2.23T \tag{9}$$

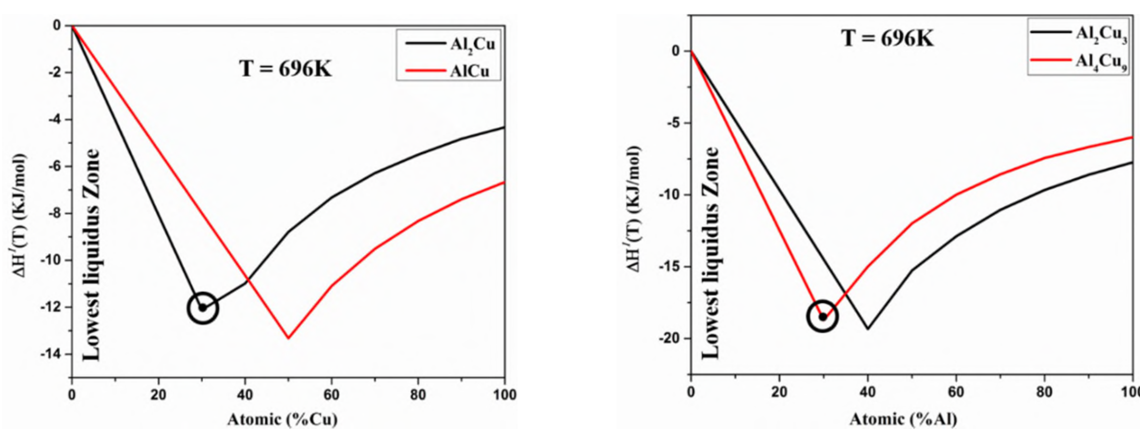

(a) **(b)**

Fig 10. Effective heat of formation at a temperature of 696 K (a) Cu as limiting element, (b) Al as limiting element

The $\Delta H'(T)$ curves for IMC Al_2Cu, $AlCu$, Al_2Cu_3, and Al_4Cu_9 are shown in Fig 10 (a) and (b) at a temperature of 696 K (peak temperature for the sample S_9). As Cu is a limiting element, the Al_2Cu IMC is observed at the lowest liquidus zone, so Al_2Cu is predicted to be earlier than AlCu, using the E_{HF} method. At the same time, Al_4Cu_9 is found to be formed earlier when Al is a limiting element.

[38] also explained the IMC thickness (L) varies with change in process parameters due to variation in the diffusion coefficient (D_C) and the time gap (t) when FSW sample temperature is higher than required diffusion. The relation among the three parameters is shown in Equation 10.

$$L = (D_c t)^{\frac{1}{2}} \tag{10}$$

The L for the welded samples is shown in Fig 11. At constant ω of 1600 rpm, the IMC thickness increase by 9.73% and 23.35% with an increase in v, from 60 to 120 mm/min and 120 to 200 mm/min, respectively. Besides, with an increase in ω, the L increases by 22.75 %. The L increases by 13.17%, with an increase in PD of 0.1 mm. The L varies with process parameters due to variation of heat generation during the welding process. From Fig 4, it has been observed, with an increase in heat input, the L increases. The line scanning at the weld interface has been recorded and the same is shown in Fig 11. The IMC zone is validated using the line scan analysis. The IMC zone comprises the starting point where Al and Cu profiles are tending to intersect and remain constant. The heat generated during the welding process has an impact on the diffusion of Al and Cu. In Fig 4 (a), the temperature gradient for the sample S_9 is nearly 11 sec above the diffusion starting temperature, i.e., 300 °C. The D_C for sample S_9 is 3.82e-13 m^2s^{-1} found using Equation 10, where the t in Equation 10 is considered as 11 sec. The D_C for the IMC formed in sample S_9 is calculated as mentioned in Table 3.

Table 3. The D_C for the IMC at the peak temperature generated in the sample S_9

IMC	***D_C (T)* (cm^2s^{-1})** [39]	***D_C (696 K)* (m^2s^{-1})**
Al_2Cu	$0.56 \times e^{\frac{-30500}{RT}}$	2.87e-7
AlCu	$2.2 \times e^{\frac{-35500}{RT}}$	4.76e-7
Al_2Cu_3	$2.1 \times e^{\frac{-33000}{RT}}$	7.1e-7
Al_4Cu_9	$8.5 \times e^{\frac{-32500}{RT}}$	3.03e-7

Based on the result *D_C (696 K)*, the IMC Al_2Cu is formed first in the Al side, and Al_4Cu_9 is formed on the Cu side, and with a further diffusion of Al and Cu at the weld interface, the phase AlCu is formed at the centre interface of the weld joint.

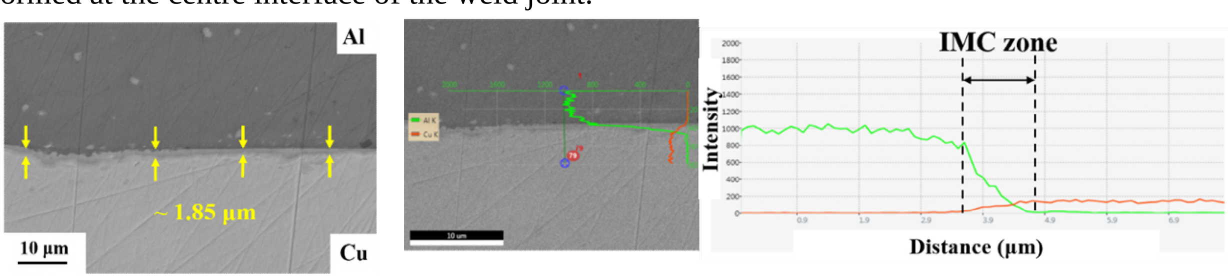

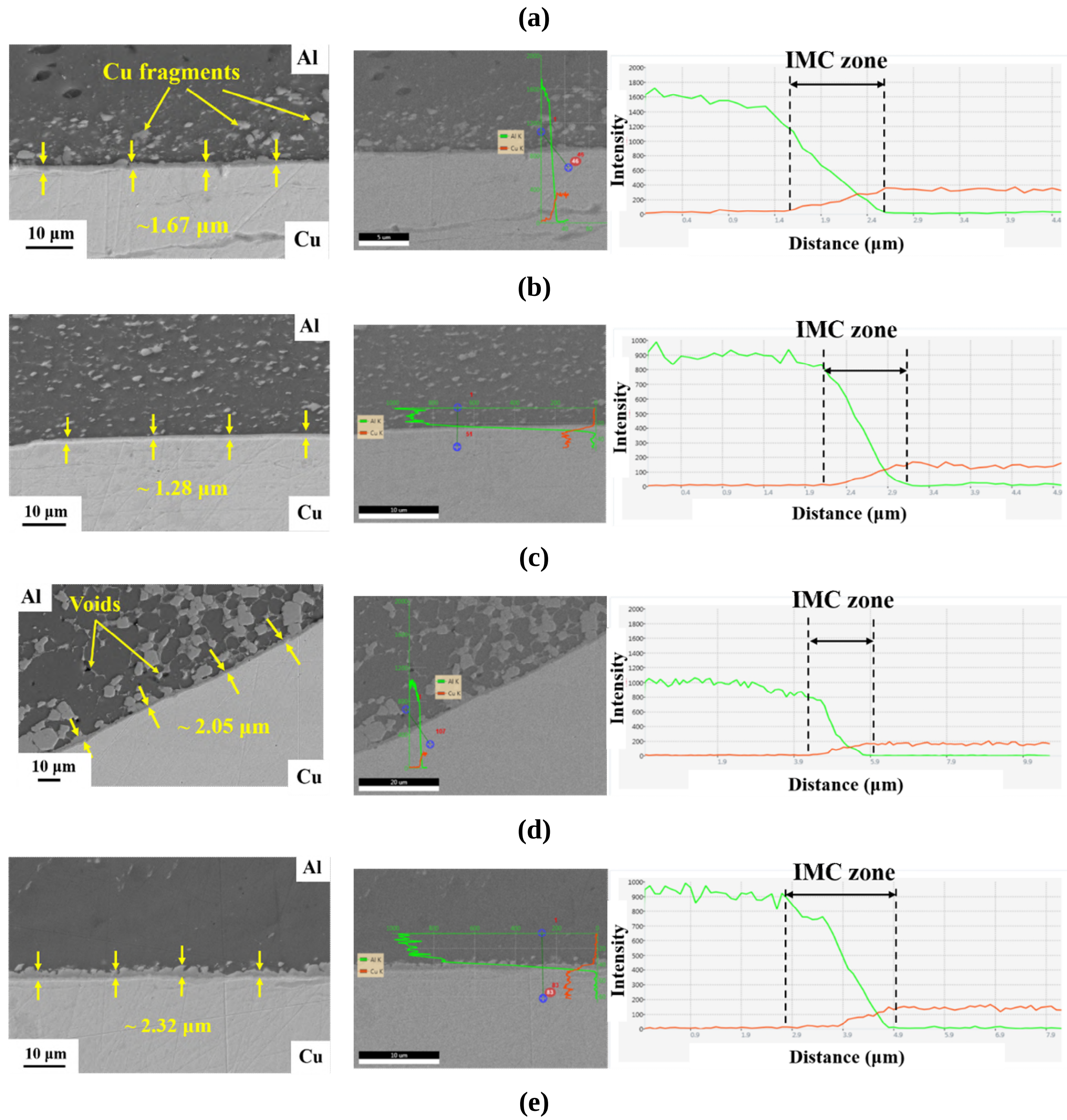

Fig 11. The micrographs images at the weld interface highlighting the IMC thickness and IMC zone of the sample, (a) S_1, (b) S_2, (c) S_7, (d) S_9, and (e) S_{11}

3.6 Nanoindentation:

The hardness at the IMC zone is measured using nanoindentation analysis. The indentation is taken in the IMC thickness zone, and Fig 12 depicts the load-displacement plot for all the samples. The formation of IMC is more at the weld nugget. Hence, the study focused on the nugget zone. The formation of major IMCs is listed in Table 4 according to the intensity obtained from the XRD analysis. Table 4 shows that the samples with lower ω have Al_2Cu as major IMC. The presence of IMC in the weld zone determines the different stress states. Fig 12 depicts those stress states, and the plot is categorized into three regions, i.e., 1) R_1: tensile stress state (L_T), 2) R_2: stress-free state (L_O), and 3) R_3: compressive stress state (L_C). The Al and samples S_1, S_2 fall under the R_1 region. The major IMC found in that sample S_1 and S_2 is Al-rich (Al_2Cu); hence, the IMC also exhibits a similar tensile stress state like Al. The samples S_3, S_4, S_5, S_7, S_8, S_9, and S_{11} show stress-free states similar to Cu, and it was found to be significant Cu-rich IMCs. Besides the samples S_6, S_{10}, and S_{12} are found with Al_4Cu_9 as the major IMC, where it undergoes the compressive stress state.

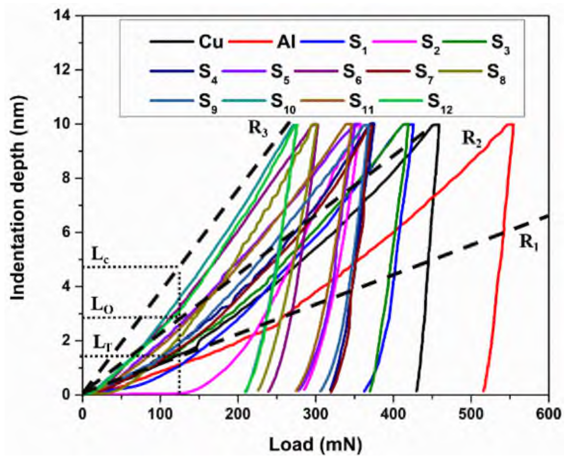

Fig 12. The load-displacement curves for the base materials and the welded samples

The deformation resistance of Cu is higher than the Al. Hence, it is observed that at the loading condition, the slope of the Cu curve is less than the Al. The lesser the slope, the higher is plastic deformation. Fig 12 depicts that all the welded samples are undergoing plastic deformation. Samples S_{10} and S_{12} are observed to be gone through severe plastic deformation due to higher ω and *PD*. The Vickers hardness (V_H) for the IMC is estimated and reported in Table 4. With an increase in v and PD, the V_H increases due to more Cu fragments in the Al-matrix. At lower ω, it has been found that Al-rich IMC (Al_2Cu) are found where at higher ω Cu-rich IMC (Al_4Cu_9) are formed. It has been observed that the Al-rich IMC is softer and has lower *E*.

A more elastic recovery has been observed in the sample under the compressive stress state, as shown in Table 4. Hence, it identified that the Al_4Cu_9 has higher hardness with less elastic deformation. Consequently, it found a higher *R*-value. The sample S_7 and S_9 have comparatively less V_H, which undergoes elastic deformation resulting in less *R* of 7.3 % and 9.7 %, respectively.

Table 4. The major IMC formed in all the welded samples, mentioning the Vickers hardness (V_H), Young's modulus (*E*), and elastic recovery (R)

Samples	**IMC***	**V_H (HV)**	***E* (GPa)**	***R* (%)**
Cu	--	167.18	127.53	5.55
Al	--	111.7	105.38	6.89

S_1	Al_2Cu; Al_2Cu_3	216.1	85.39	12.13
S_2	Al_2Cu	279.87	113.45	12.76
S_3	Al_2Cu; AlCu	223.23	88.75	13.77
S_4	Al_2Cu; AlCu	290.13	98.725	15.48
S_5	Al_2Cu; Al_4Cu_9	347.35	90.214	14.38
S_6	Al_4Cu_9; AlCu	385.31	161.22	16.89
S_7	AlCu; Al_4Cu_9	241.25	186.83	7.3
S_8	Al_4Cu_9; Al_2Cu	423.17	121.03	15.5
S_9	Al_4Cu_9; AlCu	253.78	139.66	9.7
S_{10}	Al_4Cu_9	500.08	154.43	16.76
S_{11}	AlCu	293.63	127.36	12.15
S_{12}	Al_4Cu_9	523.44	154.05	17.16

***First mentioned IMC is found as a significant composition according to the XRD analysis**

3.5 Surface roughness study

The performance of a busbar depends on the transportation of the charge carrier and the electronic parameter of a busbar material. The electronic parameters like Fermi levels, Fermi energy, and velocity need to be studied at the weld interface. The Fermi level is the variation of energy levels between the highest and lowest levels occupied by charged particles. At the absolute zero temperature, the electron attains the highest energy level and that determines the Fermi energy. Equation 11 represents the Fermi energy (E_F) calculation for a given number of free electrons (N/V).

$$E_F = \frac{\hbar}{2\, m_0} \left(\frac{3\, \pi^2\, N}{V}\right)^{\frac{2}{3}} \tag{11}$$

where, E_F = Fermi energy, ħ = Planks constant, m_0 = mass of an electron, N = number of particles and V = volume of the system

The Fermi velocity is the movement of electrons in the metals with kinetic energy associated with a Fermi energy. Equation 12 details the Fermi velocity.

$$v_F = \sqrt{\frac{2\, E_F}{m_0}} \tag{12}$$

where v_F = Fermi velocity

The electronic parameters of Cu and Al are mentioned in Table 5. These parameters are used to find a relation with the electrical resistivity for an observed root mean square (RMS) surface roughness (Δ^2). Equation 13 represents measuring an extra electrical resistivity (Δρ) using a Gaussian profile (G) value obtained for the welded samples as mentioned by [40].

$$\Delta\rho = \frac{9\,\hbar^2\Delta^2}{2\,q^2 d}\; G\left(\xi k_f\;,\;\frac{k_{ft}}{2\,k_f}\right) \tag{13}$$

where $\Delta\rho$ = extra surface electrical resistivity, Δ^2 = RMS roughness, q = charge of electron, d = thickness, G = Gaussian constant, k_{ft} = Fermi-Thomas wavelength

Equation 14 represents the calculation of k_{ft}.

$$k_{ft} = \frac{\hbar}{\sqrt{3\,m_0 K_B F_T}} \tag{14}$$

Where K_B = Boltzman constant, F_T = Fermi temperature

Table 5. Electronic parameters Fermi energy (E_F), Fermi velocity (F_v), Free electron number (N/V), Fermi temperature (F_T)

Parameters	E_F (ev)	$F_v (m/s)$	N/V ($1/m^3$)	F_T (K)
Al	11.7	2.03e+06	18.1e+28	13.6e+04
Cu	7	1.57e+06	8.47e+28	8.16e+04

The k_{ft} value for the Al and Cu, welded joints have been calculated as 5.34e-11, and the $k_{ft}/2\,k_f$ is measured as 0.4. The correlation length of the welded samples is measured and found to be 0.5 µm, i.e., average IMC thickness. The Gaussian constant, as mentioned in Equation 13, has been calculated and found to be 0.21, using a model function of the Gaussian profile as shown in Fig 13.

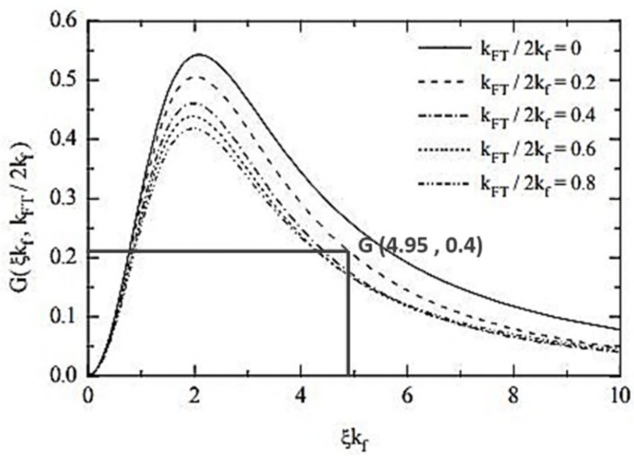

Fig 13. Gaussian profile for a scattering contribution as a function of ξk_f

The Δ^2 for the welded samples is measured by using atomic force microscopy (AFM). The Δ^2 is majorly dependent on the pit size, peak height, and the maximum number of peaks on the surface. Table 6 gives details about the maximum pit height for all the welded samples at the weld interface. The pits height defines the contact between the Al and Cu at the interface. It has been observed that the welded samples with lower ω have a maximum pit height. Moreover, the variation in process parameters differs the pit height, which could affect the electrical properties of the welded samples. The greater the pit height, the lesser the connection at the junction of Al and Cu. At lower ω, the plastic deformation of the material is less. With an increase in *PD*, the pit height decreases, implying better diffusion between Al and Cu. The samples S_9 and S_{10} have significantly less pit height, which indicates the plastic deformation is sufficient and better diffusion of Al and Cu at the interface. Besides, the presence of more peaks on the surface increases the capacitive nature, where the peaks hold the charge carriers. Moreover, the peak height directly affects the surface roughness at the welded interface. Fig 14 depicts the AFM images at the interface of all the welded samples with a scan area of 80 X 80 μm and histograms of the height of the peaks existing at the weld surface. The peak height in the weld interface zone is varying from nearly 65 nm to 550 nm. The samples S_4, S_6, S_9, and S_{10}, had less average peak height of 68.1, 116, 139, and 120, respectively, compared to other samples shown in Table 6. Among these samples, nearly 28 % of sample S_4 have a peak height within the range of 65 to 74 nm. Similarly, S_6 has a 36 % peak height in the range of 105 to 140 nm. Samples S_9 have 26 % of peak height in the range of 129 nm to 148 nm, and the 45 % peak height in the sample S_{10} has within the range of 110 nm to 130 nm. The samples S_9 and S_4 have a significantly lower percentage, which determines the charge storing, i.e., capacitive nature is minor, indicating less electrical resistivity. The Δ^2 followed an irregular trend with the process parameters as mentioned in Table 6, where the sample S_4 have a less Δ^2 of 7.37 nm, next to that, S_{10} and S_9 have 8.33 nm and 13.3 nm, respectively.

The Δρ has been calculated using Equation 13. The obtained resistivity is due to the presence of pits, peaks at the weld interface; however, the Δρ will be uniform along the weld joint. From Table 6, it has been observed that the samples that have less Δ^2 have lesser Δρ. The surface resistivity of samples S_4, S_{10}, and S_9 are found to be less, and the samples have good surface conductivity.

Table 6. Pit height (PT_h), the average peak height (P_h), RMS roughness (Δ^2), and extra surface electrical resistivity (Δρ) for the Al and Cu welded samples

Samples	PT_h (nm)	P_h (nm)	Δ^2 (nm)	Δρ (μ Ω·mm)
S_1	204	198	22.9	2.96
S_2	194	345	39.3	5.06
S_3	348	299	23.7	3.07
S_4	283	68.1	7.37	0.94
S_5	502	313	32.6	4.22
S_6	239	116	24	3.11
S_7	372	252	35	4.52
S_8	151	484	41.8	5.37
S_9	45.6	139	13.3	1.72
S_{10}	36.7	120	8.3	1.07
S_{11}	102	236	32.7	4.28
S_{12}	77.2	277	23.4	3.02

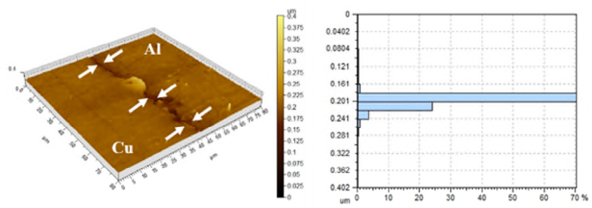

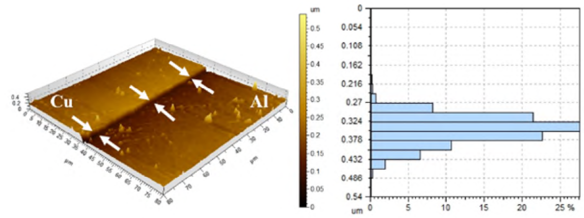

(a) **(b)**

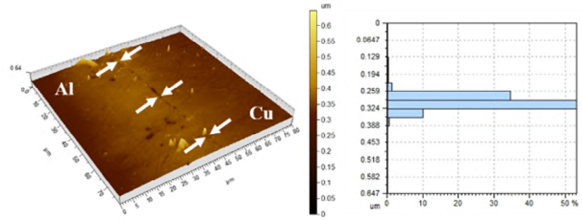

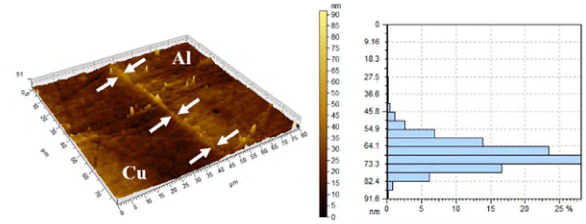

(c) **(d)**

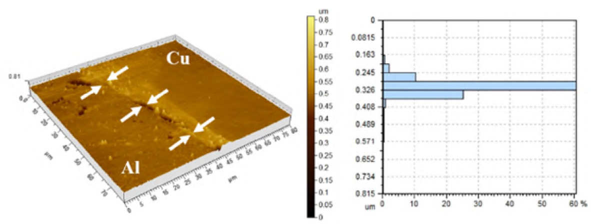

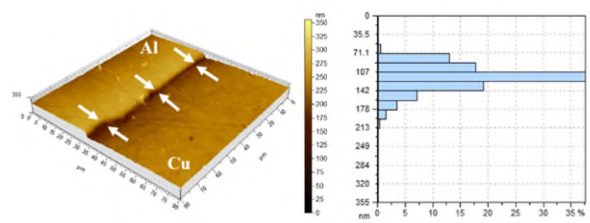

(e) **(f)**

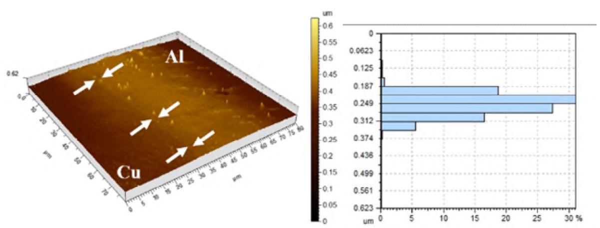

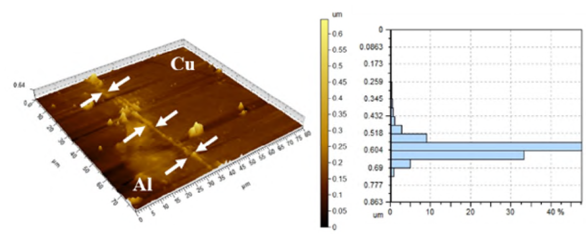

(g) **(h)**

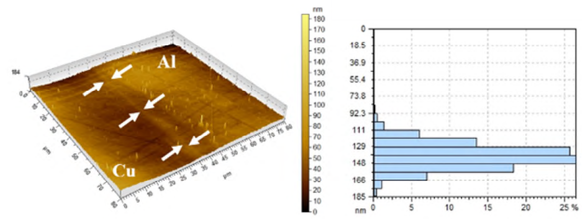

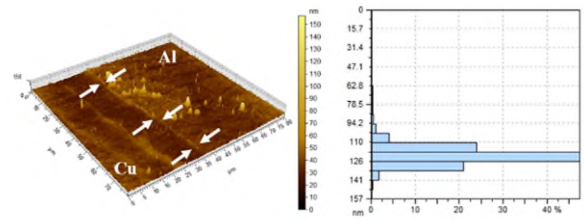

(i) **(j)**

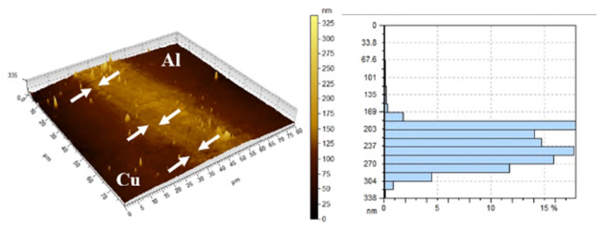

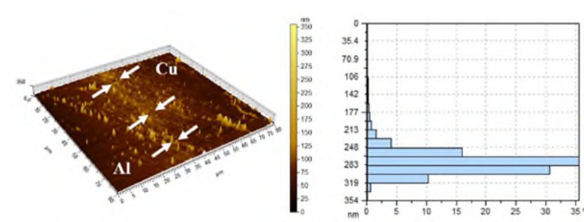

(k) **(l)**

Fig 14. Atomic force microscopy images at the weld interface of Al and Cu for the samples, (a) S_1, (b) S_2, (c) S_3, (d) S_4, (e) S_5, (f) S_6, (g) S_7, (h) S_8, (i) S_9, (j) S_{10}, (k) S_{11}, and (l) S_{12}

3.6 Electrical resistivity

The electrical resistivity of the base materials (Cu and Al) was found to be 1.32E-5 **Ω**·mm and 2.72E-5 **Ω**·mm, respectively. The electrical resistivity in the weld samples is affected significantly due to variation in the grain size, IMC formation. Further, electrical resistivity has been correlated with the vibration generated during welding. According to electronic theory, the conductivity of metals is the effective number of electrons in a free state and the mean free path of electrons. The free electrons in the lattice are the reason for good conductive metals like Ag, Cu, and Al. The mean free path of electrons is hindered by alloying, plastic deformation, and IMC formation. Among them, Cu-rich IMCs are responsible for good electric properties. The IMCs had more electrical resistivity than Cu and Al metals due to alloying of the compound. Fig 15 (a) depicts the welded samples obtained with electrical conductivity at 300 K. The samples S_2 and S_9 are found with lower and higher conductivity of 2.15 E4 S/cm and 3.21 E4 S/cm, respectively. At 300 K, the electrical resistivity of samples S_1 and S_7 was 3.86 E-5 mm and 3.98 E-5 mm, respectively. Because of the formation of optimum grain sizes, sample S_7 has a higher resistivity. The electrical resistivity increases with increasing PD. Sample S_2 had a resistivity of 4.45 E-5 mm and sample S_1 had a resistivity of 3.86 E-5 mm. The electrical resistivity has been decreased with an increase in *v*, which was due to less heat generation. The same has been observed for the samples S_3 and S_5, i.e., 3.62 E-5 **Ω**·mm and 3.44 E-5 **Ω**·mm, respectively. Similarly, sample S_9 had lower resistivity of 2.93 E-5 **Ω**.mm than sample S_{11} of 3.75 E-5 **Ω**·mm. The lower resistivity of sample S_9 was observed due to the formation of more Cu-rich IMCs, i.e., Al_4Cu_9 and AlCu. Moreover, sample S_9 experiences a higher intensity of vibrations during the welding process, as shown in Fig 6 (d). The optimum heat generation and vibration lead to good material mixing of Cu fragments in Al matrix, leading to Cu-rich IMCs.

Moreover, the sample S_9 was observed to be having higher UTS, which is also a defect-free weld, i.e., free from voids. The resistivity of the sample S_9 had 7.3% more than the resistivity of Al, which is near to Al resistivity as compared to other welded samples. Hence this process parameter is suitable for the joining of Al-Cu in busbar applications. The main concern about the battery application while in running conduction of EVs, the busbars are subjected to heat up to a maximum temperature of nearly about 323 K. Hence, the study of resistivity at extreme conditions is essential. Thus, the welded samples are tested in a high-temperature resistivity test ranging from 300 K to 345 K.

According to electronic theory, with the increase in temperature of a conductor, the vibrations of metal ions also increase. These vibrations result in a collision between free electrons and other electrons. These collisions decrease the energy of free electrons and make them reach the static state of electrons. Hence, the delocalized electrons present in the static state are restricted from moving, leading to the rise in the electric resistivity of a conductor. The increase in resistivity with an increase in the temperature is the basic property of the conductive materials. Fig 15 (b) represents that the electrical resistivity increases with the increase in temperature, indicating the welded zone also exhibits conductor behaviour. The samples S_2, S_3, S_5, and S_9 had less resistivity of 6.66 E-5 Ω·mm, 5.07 E-5 Ω·mm, 4.33 E-5 Ω·mm, and 3.35 E-5 Ω·mm, respectively at a temperature of 345 K. Among them, the percentage change in resistivity is lesser for samples S_5 and S_9 is 25.8 %, and 14.7 %, respectively from temperature 300 K to 345 K. Hence, it has been concluded that sample S_9 has better electrical properties at the higher temperature, which is required for battery applications.

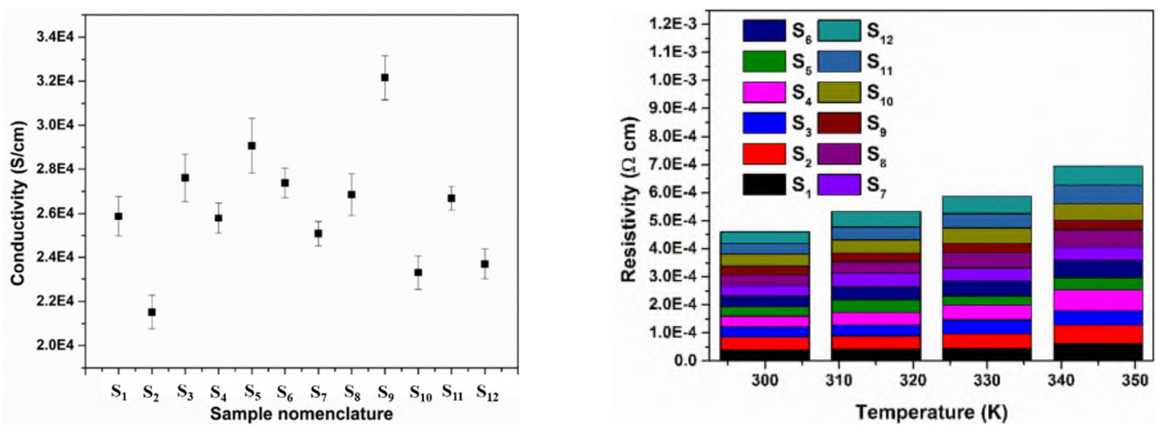

(a) (b)

Fig 15. (a) Electrical conductivity of different welded samples at 300 K, and (b) variation of electrical resistivity of the welded samples at a different temperature from 300 K to 345 K

4 Conclusion

The automobile industry requires a Li-ion battery pack with full efficiency of power supply for EVs. Such a requirement needs an effective Al-Cu busbar joining without defects and voids. FSW, being a solid-state joining process, has been used mostly over fusion welding. The weld quality is assessed by mechanical and metallurgical investigations like UTS and interface grain size, microhardness, IMC thickness, and IMC hardness. The formation of IMCs is affecting the mechanical and electrical properties. The following conclusions are drawn as follows:

1) The Al-Cu busbar fabricated by FSW, with higher ω, experienced a severe plastic deformation favourable for Cu-rich IMCs like Al_2Cu_3 and Al_4Cu_9, leading to increased joint strength.

2) The vibrations generated due to higher *v* leads to the formation of more Al_4Cu_9 IMC. The Al_4Cu_9 IMC is Cu-rich, which enhances the tensile strength and electrical properties.

3) The samples S_9 and S_{10} has high plastic deformation observed less pit height indicates less RMS surface hardenss Δ^2 which leads to lesser surface resisitivity $\Delta\rho$.

4) The sample with ω of 2400 rpm, *v* at 120 mm/min, and a PD of 0.2 mm has been observed to be having a maximum UTS due to the formation of Cu-rich IMC. Because of this, it has a lower electrical resistivity of 2.93 E-5 Ω.mm due to good mechanical bonding and defect-free weld. Moreover, this sample maintained a minor increment of 14.7% in electrical resistivity from room temperature to 345 K.

Contributions

Methodology: Surjya Kanta Pal; experimental work: Omkar Mypati, Suryakanta Sahu; data analysis: Omkar Mypati; writing the first draft: Omkar Mypati, Suryaknata Sahu; writing, review, and editing: Omkar Mypati, Surjya Kanta Pal. All authors have read and agreed to the published version of the manuscript.

Corresponding author

Correspondence to **Surjya Kanta Pal**.

Ethics declarations

Ethics approval

Not applicable

Consent to participate

Not applicable

Consent for publication

Not applicable

Competing interests

The authors declare no competing interests.

Availability of data and materials

All the data and material are available upon request to the corresponding author.

References

1. Faria R, Moura P, Delgado J, Almeida AT De (2012) A sustainability assessment of electric vehicles as a personal mobility system. Energy Convers Manag 61:19–30. https://doi.org/10.1016/j.enconman.2012.02.023

2. Becker J, Nemeth T, Raphael W, Dirk, Uwe S (2018) Dimensioning and Optimization of Hybrid Li-Ion Battery Systems for EVs. World Electr Veh J 9:. https://doi.org/10.3390/wevj9020019

3. Andrea, Aurora R, Inut M, Sergiu-Dan S (2015) A look into electric/hybrid cars from an ecological perspective. Procedia Technol 19:438–443. https://doi.org/10.1016/j.protcy.2015.02.062

4. Das A, Dezhi L, David W, David G (2018) Joining Technologies for Automotive Battery Systems Manufacturing. World Electr Veh J 9:1–13. https://doi.org/10.3390/wevj9020022

5. Burke AF (2007) Batteries and ultracapacitors for electric, hybrid, and fuel cell vehicles. Proc IEEE 95:806–820. https://doi.org/10.1109/JPROC.2007.892490

6. Feng F, Northwood DO (2005) Self-discharge characteristics of a metal hydride electrode for Ni-MH rechargeable batteries. Int J Hydrogen Energy 30:1367–1370. https://doi.org/10.1016/j.ijhydene.2005.06.013

7. Kouchachvili L, Yaïci W, Entchev E (2018) Hybrid battery / supercapacitor energy storage system for the electric vehicles. J Power Sources 374:237–248. https://doi.org/10.1016/j.jpowsour.2017.11.040

8. Mypati O, Mishra D, Sahu S, et al (2019) A Study on Electrical and Electrochemical Characteristics of Friction Stir Welded Lithium-Ion Battery Tabs for Electric Vehicles. J Electron Mater. https://doi.org/10.1007/s11664-019-07711-8

9. Miao Y, Hynan P, Von Jouanne A, Yokochi A (2019) Current li-ion battery technologies in electric vehicles and opportunities for advancements. Energies 12:1–20. https://doi.org/10.3390/en12061074

10. Chen X, Shen W, Vo TT, et al (2012) An overview of lithium-ion batteries for electric vehicles. 10th Int Power Energy Conf IPEC 2012 230–235. https://doi.org/10.1109/ASSCC.2012.6523269

11. Koktsinskaya EM, Roshal AG, Karpishin VM, Prosvirnin VG (2014) Aging tests of the high current aluminum-copper contact connections in the ITER DC busbar system. IEEE Trans Plasma Sci 42:443–448. https://doi.org/10.1109/TPS.2013.2290703

12. Mypati O, Pal SK, Srirangam P A Study on Electrical Conductivity of Micro Friction Stir-Welded Dissimilar Sheets for Hybrid Electric Vehicles (HEVs). Springer International Publishing

13. Bao Y., Cheng KWE, Ding K, Wang DH The Study on the Busbar System and its Fault Analysis. 2013 5th Int Conf Power Electron Syst Appl 1–7. https://doi.org/10.1109/PESA.2013.6828246

14. Ghareeb Moustafa, Grossmann S, Salam, Mazen Abdel, S. S. Dessouky SME (2009) Joint Resistance of Bolted Copper Bus - Bar Connections as influenced by Mechanical Contact Devices Material and Configuration. 300–305

15. Schneider, R. ; Löbl, H.; Grossmann, S. ; Schoenemann, T. ; Holdis M (2009) Long-term behavior of aluminum-copper Connections in electrical energy technology. Metall 63:591–594

16. Gulenc B (2008) Investigation of interface properties and weldability of aluminum and copper plates by explosive welding method. Mater Des 29:275–278. https://doi.org/10.1016/j.matdes.2006.11.001

17. Kaspar J, Zimmermann M, Ostwaldt A, et al (2014) Challenges in joining aluminium with copper for applications in electro mobility. Mater Sci Forum 783–786:1747–1752. https://doi.org/10.4028/www.scientific.net/msf.783-786.1747

18. Meng X, Huang Y, Cao J, et al (2021) Recent progress on control strategies for inherent issues in friction stir welding. Prog Mater Sci 115:100706. https://doi.org/10.1016/j.pmatsci.2020.100706

19. Ji F, Xue SB, Lou JY, et al (2012) Microstructure and properties of Cu/Al joints brazed with Zn-Al filler metals. Trans Nonferrous Met Soc China (English Ed 22:281–287. https://doi.org/10.1016/S1003-6326(11)61172-2

20. Lee SJ, Nakamura H, Kawahito Y, Katayama S (2014) Effect of welding speed on microstructural and mechanical properties of laser lap weld joints in dissimilar Al and Cu sheets. Sci Technol Weld Join 19:111–118. https://doi.org/10.1179/1362171813Y.0000000168

21. Weigl M, Schmidt M (2009) Modulated laser spot welding of dissimilar copper-aluminium connections. Int Conf Multi-Material Micro Manuf 4M/International Conf Micro Manuf ICOMM 211–214. https://doi.org/10.1243/17547164C0012009040

22. Kah P, Rajan R, Martikainen J, Suoranta R (2015) Investigation of weld defects in friction-stir welding and fusion welding of aluminium alloys. Int J Mech Mater Eng 10:. https://doi.org/10.1186/s40712-015-0053-8

23. Mypati O, Sadhu A, Sahu S, Mishra D (2019) Enhancement of joint strength in friction stir lap welding between AA6061 and AISI 304 by adding diffusive coating agents. 1–14. https://doi.org/10.1177/0954405419838379

24. Mishra RS, Ma ZY (2005) Friction stir welding and processing. Mater Sci Eng R Reports 50:1–78. https://doi.org/10.1016/j.mser.2005.07.001

25. Akbari M, Abdi Behnagh R, Dadvand A (2012) Effect of materials position on friction stir lap welding of Al to Cu. Sci Technol Weld Join 17:581–588. https://doi.org/10.1179/1362171812Y.0000000049

26. Mao A, Zhang J, Yao S, et al (2020) The diffusion behaviors at the Cu-Al solid-liquid interface: A molecular dynamics study. Results Phys 16:. https://doi.org/10.1016/j.rinp.2020.102998

27. Mahto RP, Bhoje R, Pal SK, et al (2016) A study on mechanical properties in friction stir lap welding of AA 6061-T6 and AISI 304. Mater Sci Eng A 652:136–144. https://doi.org/10.1016/j.msea.2015.11.064

28. Gulyaev AP, Sarmanova LM (1972) High-temperature plasticity of carbon steels. Met Sci Heat Treat 14:329–332. https://doi.org/10.1007/BF00657023

29. Nandan R, Debroy T, Bhadeshia HKDH (2008) Recent Advances in Friction Stir Welding – Process , Weldment Structure and Properties. 53:980–1023

30. Rajesh S, Badheka VJ (2018) Process parameters/material location affecting hooking in friction stir lap welding: Dissimilar aluminum alloys. Mater Manuf Process 33:323–332. https://doi.org/10.1080/10426914.2017.1317798

31. Wang M, Zhang H, Zhang J, et al (2014) Effect of pin length on hook size and joint properties in friction stir lap welding of 7B04 aluminum alloy. J Mater Eng Perform 23:1881–1886. https://doi.org/10.1007/s11665-014-0936-5

32. Vladimirov I, Kühn M, Geßner T, et al (2018) Energy barriers at grain boundaries dominate charge carrier transport in an electron-conductive organic semiconductor. Sci Rep 8:1–10. https://doi.org/10.1038/s41598-018-33308-y

33. Xue P, Xiao BL, Wang D, Ma ZY (2011) Achieving high property friction stir welded aluminium/copper lap joint at low heat input. Sci Technol Weld Join 16:657–661. https://doi.org/10.1179/1362171811Y.0000000018

34. Abdollah-Zadeh A, Saeid T, Sazgari B (2008) Microstructural and mechanical properties of friction stir welded aluminum/copper lap joints. J Alloys Compd 460:535–538. https://doi.org/10.1016/j.jallcom.2007.06.009

35. Saeid T, Abdollah-zadeh a., Sazgari B (2010) Weldability and mechanical properties of dissimilar aluminum-copper lap joints made by friction stir welding. J Alloys Compd 490:652–655. https://doi.org/10.1016/j.jallcom.2009.10.127

36. Elrefaey A, Takahashi M, Ikeuchi K (2005) Preliminary Investigation of Friction Stir Welding Aluminium/Copper Lap Joints. Weld World 49:93–101. https://doi.org/10.1007/BF03266481

37. Galvão I, Verdera D, Gesto D, et al (2013) Influence of aluminium alloy type on dissimilar friction stir lap welding of aluminium to copper. J Mater Process Technol 213:1920–1928. https://doi.org/10.1016/j.jmatprotec.2013.05.004

38. Wang T, Sidhar H, Mishra RS, et al (2019) Evaluation of intermetallic compound layer at aluminum/steel interface joined by friction stir scribe technology. Mater Des 174:107795. https://doi.org/10.1016/j.matdes.2019.107795

39. Yasuhiro Funamizu and Katsuya Watanabe (1971) Interdiffusion in the Al-Cu System. Mater Trans 12:

40. Ketenoğlu D, Ünal B (2013) Influence of surface roughness on the electrical conductivity of semiconducting thin films. Phys A Stat Mech its Appl 392:3008–3017. https://doi.org/10.1016/j.physa.2013.03.007